ACS APPLIED MATERIALS & INTERFACES

Research Article

Cite This: ACS Appl. Mater. Interfaces 2019, 11, 19286−19293

www.acsami.org

Controllable Synthesis of Monodispersed $Fe_{1-x}S_2$ Nanocrystals for High-Performance Optoelectronic Devices

Maogang Gong,*,† Dan Ewing,‡ Matthew Casper,‡ Alex Stramel,‡ Alan Elliot,‡ and Judy Z. Wu*,†

†Department of Physics and Astronomy, University of Kansas, Lawrence, Kansas 66045, United States

‡Department of Energy's National Security Campus, Kansas City, Missouri 64147, United States

Supporting Information

ABSTRACT: The optical properties of stoichiometric iron pyrite (FeS_2) nanocrystals (NCs) are characterized by strong UV−Visible (UV−Vis) absorption within the cutoff while negligible absorption beyond the cutoff in near-infrared and longer wavelengths. Herein, we show this bandgap limitation can be broken through controllable synthesis of nonstoichiometric $Fe_{1-x}S_2$ NCs (x = 0.01−0.107) to induce localized surface plasmonic resonance (LSPR) absorption beyond the cutoff to short-wave infrared spectrum (SWIR, 1−3 μm) with remarkably enhanced broadband absorption across UV−Vis−SWIR spectra. To illustrate the benefit of the broadband absorption, colloidal LSPR $Fe_{1-x}S_2$ NCs were printed on graphene to form LSPR $Fe_{1-x}S_2$ NCs/graphene heterostructure photodetectors. Extraordinary photoresponsivity in exceeding 4.32×10^6 A/W and figure-of-merit detectivity $D^* > 7.50 \times 10^{12}$ Jones have been demonstrated in the broadband of UV−Vis−SWIR at room temperature. These $Fe_{1-x}S_2$ NCs/graphene heterostructures are printable and flexible and therefore promising for practical optical and optoelectronic applications.

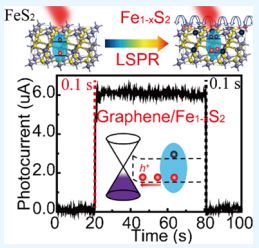

KEYWORDS: *nonstochiometric nanocrystals, graphene, pyrite, carrier doping, van der Waals heterojunction, optoelectronics*

1. INTRODUCTION

Localized surface plasmonic resonance (LSPR) provides a unique approach to enhance light-solid interaction and has been studied extensively in metal nanostructures.[1−4] Upon light illumination, free electrons oscillate collectively on the surface of the metal nanostructures at the LSPR frequencies that are determined by free carrier concentration, shape, and dimension of the metal nanostructures, resulting in a broad application of metallic LSPR nanostructures in photocatalysis, biosensing, photodetection, photovoltaics, etc.[5−13] Semiconductor LSPR nanocrystals (NCs) are promising in optical and optoelectronic applications due to their advantages in enhanced light absorption and spectral tunability.[14−18] Specifically, the semiconductor LSPR NCs allow enhanced light absorption in a wide spectral range much beyond the original bandgap limitation.[14,19,20] However, the LSPR effect is negligible in intrinsic semiconductors due to their low charge carrier densities.[20−22] Controllable carrier doping is therefore critical to realization of the LSPR effect in semiconductor NCs.[19,23]

Colloidal semiconductor NCs are particularly suitable to exploration of semiconductor LSPR NCs due to multiple advantages including low fabrication costs and controllability of the nanocrystal's composition, shape, and dimension. In particular, carrier doping of the colloidal semiconductor NCs can be readily achieved by controlling their chemical composition using selected precursor solutions. When the dimension of the semiconductor NCs is restricted in a few to few tens of nanometers, the much enhanced LSPR light-solid interaction can be combined with the strong quantum confinement in semiconductor NCs to provide unique advantages for photonic and optoelectronic applications. Motivated by this, several groups have recently reported synthesis of colloidal LSPR semiconductor NCs with controlled sizes,[22,24,25] shapes,[25,26] and composition.[20,27] For example, doping of Cu-based semiconductor NCs ($Cu_{2-x}S$ or $Cu_{2-x}Se$) through variation the elemental ratio of Cu and S (or Se) has illustrated the LSPR effect-induced broadening of the absorption spectra from originally visible to near-infrared (NIR, 800−1000 nm) spectrum.[14,19,22]

Iron pyrite (FeS_2), another representative transition metal chalcogenide, is an attractive semiconductor used as the active layer in photoelectrochemical and photovoltaic cells.[28−30] FeS_2 has a remarkably high optical absorption coefficient exceeding 10^5 cm^{-1} and sufficiently long minority carrier diffusion length (100−1000 nm), both of which are important to optoelectronic applications.[31,32] In the bulk form, FeS_2 has a bandgap of ∼0.95 eV in a visible spectrum. A blue-shifted bandgap of 1.0−1.58 eV was reported in stoichiometric FeS_2 NCs of small dimension on the order of 2−30 nm due to the strong quantum confinement.[15,33,34] In contrast, a red shift of the absorption spectrum was observed on larger stoichiometric FeS_2 nanocubes of dimension in the range of 50−150 nm at which the quantum confinement is no longer important. While surface/interface defects are hypothesized to provide carrier doping in the FeS_2 nanocubes, the mechanism responsible for the observed broadband light absorption and its correlation with the LSPR effect remains unclear.[15,35,36] Consequently,

Received: March 8, 2019
Accepted: May 7, 2019
Published: May 7, 2019

DOI: 10.1021/acsami.9b04250
ACS Appl. Mater. Interfaces 2019, 11, 19286−19293

controlling the LSPR effect in terms of the spectral range and enhancement factor of the light absorption remains difficult.

In this work, a colloidal process was developed for synthesis of nonstoichiometric $Fe_{1-x}S_2$ NCs to induce direct carrier doping in $Fe_{1-x}S_2$ NCs of 10−60 nm by varying x in the range of $x = 0.01-0.107$. Remarkably, the doped $Fe_{1-x}S_2$ NCs exhibit a pronounced LSPR effect with absorption spectra extended systematically from visible to short-wave infrared (SWIR, 1−3 μm) spectrum with increasing excess holes doped to the valence band by the induced iron deficiencies. To demonstrate the advantage of the LSPR $Fe_{1-x}S_2$ NCs in optoelectronic devices, photodetectors based on van de Waals (vdW) heterostructures of the LSPR $Fe_{1-x}S_2$ NCs printed onto the channel of graphene field-effect transistors (GFETs) were constructed. We show that the enhanced LSPR absorption of the $Fe_{1-x}S_2$ NCs can be transduced to the photodetectors, leading to LSPR-enabled high photoresponsivity in the broadband of ultraviolet−visible−near-infrared (UV−Vis−SWIR). This result illustrates that the doped $Fe_{1-x}S_2$ NCs are excellent LSPR photosensitizers with both spectral tunability and enhanced light-solid interaction.

2. EXPERIMENTAL SECTION

2.1. $Fe_{1-x}S_2$ NCs. The $Fe_{1-x}S_2$ colloidal NCs were fabricated using a solvothermal route in a Schlenk-line system. In detail, $FeCl_2$ (0.5 mmol) and octadecylamine (ODA, 12 g) were added into a round-bottom three-neck flask under ambient atmosphere and then vacuumized/refilled with Ar for 10 min in a Schlenk-line system for the chemical reaction at an inert gas environment. Then, the temperature was increased to 120 °C for 2 h for decomposition of the chemicals. Meanwhile, 4 mmol of sulfur powder and 5 mL of diphenyl ether were added into the second round-bottom three-neck flask and sonicated for 10 min in an ultrasound sonicator. Similar degassing process was done in the Schlenk-line system. The sulfur mixture was heated to 70 °C for 1 h as a sulfur-diphenyl ether precursor, which was quickly injected into the first Fe-ODA precursor flask at 220 °C and kept at this temperature for 90 min. The element ratio of Fe to S in $Fe_{1-x}S_2$ NCs should be tuned by changing the chemical stoichiometry; for example, the Fe/S ratio was adjusted from 0.99:2 to 0.952:2 and 0.917:2 at the chemical ratio of $FeCl_2$ to sulfur of 1:8, 1:9.6, and 1:11.2, respectively. Details are shown in Table S1 (Supporting Information). The obtained $Fe_{1-x}S_2$ NCs were cleaned and collected by a centrifuge at the speed of 4000 rpm in a glovebox filled with N_2.

2.2. $Fe_{1-x}S_2$ NCs/GFET Photodetector Fabrication. Graphene field-effect transistors (GFETs) with different sizes of monolayer graphene channels were fabricated using a previously reported method.[37,38] The $Fe_{1-x}S_2$ NCs were dissolved in chloroform at the concentration of 25 mg/mL and were used as the printing ink, which was printed on the GFET channels by using an printer (inkjet microplotter, SonoPlot, Inc.). The printed $Fe_{1-x}S_2$ NCs/GFET photodetectors were stored in a glovebox filled with N_2 and naturally dried at room temperature for 20 min.

2.3. Surface Treatment. The surfaces of as-synthesized $Fe_{1-x}S_2$ NCs absorbed a layer of insulating long carbon chains molecular ODA, which formed a charge transfer barrier in the contact interfaces among NCs or NC electrodes. These insulating layers induced by the organic solvent could be removed and substituted by a conductive molecular of 3-mercaptopropionic acid (MPA). The MPA surface engineering solution was prepared by mixing MPA with methanol (v/v = 1:1). The printed $Fe_{1-x}S_2$ NCs/GFET devices were submerged into the MPA solution for 90 s and then rinsed using methanol to clean the MPA residuals on the surface of the device. The surface-engineered devices were stored in a glovebox for 10 min to evaporate the treated solutions. Finally, these devices were packed by a thin layer of PMMA (polymethyl methacrylate) to avoid oxidation in air.

2.4. Materials and Devices Characterization. The optical absorption properties of $Fe_{1-x}S_2$ NCs were characterized using a UV-3600 Shimadzu spectrophotometer. The morphology and crystal structure of $Fe_{1-x}S_2$ NCs were taken via a field-emission FEI Tecnai F20XT. The optoelectronic properties of $Fe_{1-x}S_2$ NCs/GFET photodetectors were characterized on a semiconductor device analyzer (Agilent B1505A). The tunable light source was provided by an optical system comprised of a xenon lamp and a monochromator (Newport). The device size was tested by optical microscopy (Nikon Eclipse LV 150 with a CCD camera). A broad beam light source was employed, so the light-spot size was considerably larger than the active area of the photodetector to ensure uniform illumination of the device. In this case, the real light energy absorption area is determined by the device area of 4.3 μm (length) × 11.4 μm (width). A Stanford Research SR 760 spectrum analyzer was used to measure the noise signal of the photodetectors.

3. RESULTS AND DISCUSSION

The crystalline structure of FeS_2 can be best described in terms of sodium chloride (NaCl) with the centers of gravity of sulfur atom pairs and the sublattices occupied by iron atoms. The crystal structure of stoichiometric FeS_2 with perfect elemental stoichiometry of 1:2 is shown in Figure 1a. This type of iron pyrite demonstrates the intrinsic semiconductor property with a bandgap of ~0.95 eV[33] and negligible LSPR effect due to a low free carrier concentration. Figure 1b depicts the crystal structure of doped $Fe_{1-x}S_2$ with iron deficiencies, which

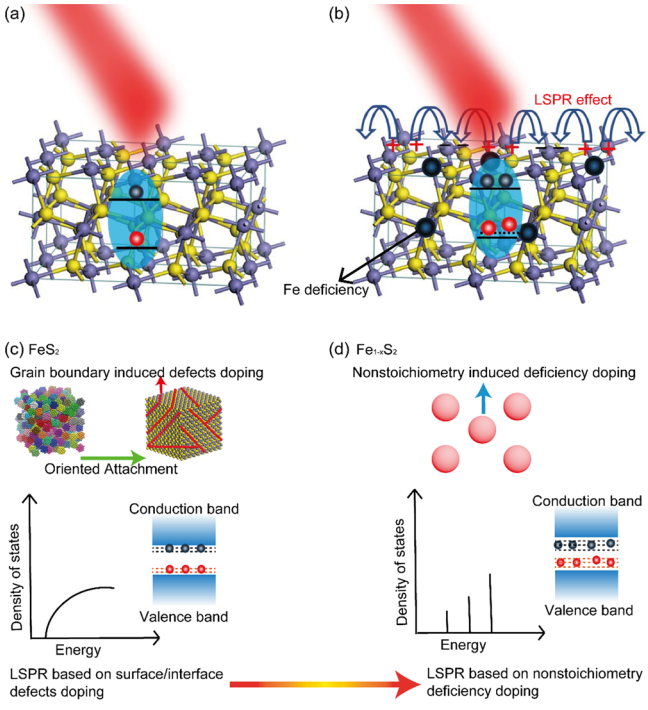

Figure 1. Crystal structure of (a) stoichiometric FeS_2 exhibiting traditional semiconducting property under light irradiation and (b) $Fe_{1-x}S_2$ with Fe deficiencies, which induce hole charge carriers for the LSPR effect under broadband light irradiation. Iron, sulfur atoms, and iron deficiencies are depicted as violet, yellow, and black balls, respectively. (c) LSPR effect based on surface/interface defects doping in FeS_2 nanocubes, grown by oriented attachment of small-size FeS_2 NCs with the induced defective interface defects shown using red lines. (d) LSPR effect based on controllable nonstoichiometry deficiency doping in $Fe_{1-x}S_2$ NCs. The insets are representative schematics of energy band and density of states in one energy band of (c) FeS_2 nanocubes and (d) $Fe_{1-x}S_2$ NCs.

DOI: 10.1021/acsami.9b04250
ACS Appl. Mater. Interfaces 2019, 11, 19286−19293

becomes p-type due to the hole doping in the valence band. These free-carrier holes resonate to produce the LSPR effect in the $Fe_{1-x}S_2$ NCs under light excitation, and the LSPR effect can be quantitatively controlled by the hole-doping level. The LSPR effect is expected to red-shift the spectral range of optical absorption with a much enhanced absorption amplitude.[14,23] Figure 1c describes the difference in the LSPR effect of the stoichiometric FeS_2 nanocubes and nonstoichiometric $Fe_{1-x}S_2$ NCs. Since the stoichiometric FeS_2 nanocubes are formed via oriented-attachment growth of many smaller-size FeS_2 NCs, as shown in Figure 1c, a large amount of defective interfaces form after the NCs merge.[34] Considering that such defect-induced doping is not uniform at an atomic scale, a weak and uncontrollable LSPR effect is anticipated in the stoichiometric FeS_2 nanocubes.[36] In contrast, the nonstoichiometry $Fe_{1-x}S_2$ NCs can exhibit a much stronger LSPR effect ascribing to the high carrier doping uniform at an atomic scale that is induced by the Fe deficiencies in each unit cell through composition control. In fact, the estimated carrier density in $Fe_{1-x}S_2$ NCs could be up to 1.91×10^{22} cm^{-3} (Supporting Information). In addition, the coupling of LSPR and quantum confinement in $Fe_{1-x}S_2$ NCs can further enhance the photoconductive gain in optoelectronic devices,[14] as shown in the comparison of the performance of the FeS_2/GFET photodetectors using stoichiometric FeS_2 nanocubes or nonstoichiometric $Fe_{1-x}S_2$ NCs as photosensitizers, respectively (Table S2 and discussion below).

Figure 2a,b shows the transmission electron microscopy (TEM) images of well-dispersed $Fe_{1-x}S_2$ NCs with the ratios of Fe to S of 0.99:2 and 0.917:2, respectively. The size distributions are also illustrated for these two samples in the same figures. The TEM images and size distributions of two other samples with Fe/S ratios of 0.962:2 and 0.952:2 are shown in Figure S1. Most $Fe_{1-x}S_2$ NCs have an irregular shape with a comparable average size of 25−30 nm. This means that the LSPR frequency is primarily dependent on the stoichiometry of the $Fe_{1-x}S_2$ NCs with a negligible size effect between the NCs of different chemical compositions. The chemical composition of $Fe_{1-x}S_2$ was analyzed using energy dispersive X-ray spectroscopy (EDS) in the TEM. Figure 2c,d depicts the high-resolution TEM (HRTEM) images corresponding to the samples in Figure 2a,b, respectively. High crystallinity was demonstrated in both $Fe_{1-x}S_2$ NC samples, and they both have a lattice fringe of ∼0.27 nm, which is close to the anticipated value for the (200) planes of the iron pyrite.[39]

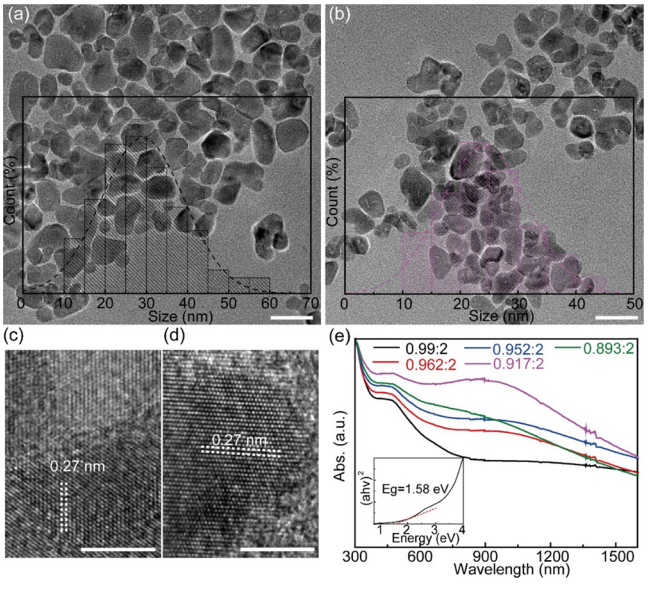

Figure 2. (a, b) TEM images of $Fe_{1-x}S_2$ NCs with different chemical compositions (Fe/S ratios: (a) 0.99:2 and (b) 0.917:2). The insets show the corresponding size distribution histogram. The scale bars are 50 nm. (c, d) HRTEM images corresponding to samples in (a) and (b), respectively. The scale bars are 5 nm. (e) UV−Vis−IR absorption spectrum of $Fe_{1-x}S_2$ NCs with different elemental ratios. The inset shows the Tauc plot measurement obtained from the bandgap of $Fe_{0.99}S_2$ NC thin film.

The UV−Vis−IR absorption spectra of $Fe_{1-x}S_2$ NCs are demonstrated in Figure 2e. The carrier doping-induced LSPR effect is clearly shown to lead to the appearance of an IR band systematically with decreasing Fe/S ratio. The stoichiometric $Fe_{0.99}S_2$ NCs (black) have an absorption cutoff of ∼785 nm that corresponds to the bandgap of 1.58 eV based on the Tauc plot[33,40] $\alpha h\nu \propto (h\nu - E_g)^{1/2}$ (inset of Figure 2e), where α is the absorption coefficient, $h\nu$ is the photo energy, and E_g is the bandgap. The blue shift of the bandgap from the bulk value is anticipated for the $Fe_{1-x}S_2$ NCs due to the quantum confinement. With increasing carrier doping through the introduction of Fe vacancies in the $Fe_{1-x}S_2$ NCs, the induced LSPR effect leads to a systematic development of an IR absorption band spanning over NIR and SWIR spectra, which gains systematically not only in the absorption intensity but also in spectral broadening through a red shift with decreasing Fe/S ratio up to 0.917:2. At a 900 nm wavelength, for example, the absorption intensity increases monotonically with decreasing Fe/S ratio from stoichiometric 0.99:2 (black) to 0.917:2 (purple) due to increasing hole concentration. This observation is in excellent agreement with recent studies of the LSPR effect in other doped semiconductor NCs of $Cu_{2-x}S$,[14] $Cu_{2-x}Se$,[19] $Cu_{2-x}Te$,[20] and WO_{3-x}.[41] It should be noted that the optimal LSPR effect was observed in $Fe_{1-x}S_2$ NCs at x = 0.083. A further increase in doping to the Fe/S ratio = 0.893:2 (the green curve in Figure 2e) shows a reduced absorption intensity at 900 nm, which may be ascribed to the increased light reflection as the doped $Fe_{1-x}S_2$ NCs become more metallic with higher carrier concentrations. In the following discussion, we will mainly focus on the low-doping $Fe_{1-x}S_2$ NCs with an Fe/S ratio from 0.99:2 to 0.917:2.

The LSPR-enhanced light absorption in $Fe_{1-x}S_2$ NCs makes them ideal photosensitizers for broadband photodetectors. Figure 3 depicts schematically the printing process of the $Fe_{1-x}S_2$ NCs on the channel of a GFET from an ink of $Fe_{1-x}S_2$ NCs in chloroform using a SonoPlot microplotter through a glass capillary tip. A schematic of a GFET device from a 36 GFET array chip (the real image is shown in Figure S2) is illustrated in Figure 3a. The GFETs have different channel lengths of 2−20 μm, and the same channel width of 20 μm was fabricated by transfer monolayer graphene grown in chemical vapor deposition (CVD) on SiO_2 (90 nm)/Si substrates. A two-step photolithography process was employed to define the GFET array and the Au (80 nm)/Ti (2 nm) source and drain electrodes. The Raman spectra taken on the GFET channel of a representative GFET before and after printing $Fe_{1-x}S_2$ NCs are shown in Figure S3, which confirms the high quality of the monolayer graphene, which remained intact after the $Fe_{1-x}S_2$ NC printing. The $Fe_{1-x}S_2$ NC ink can be controllably printed on the GFET channel since the inkjet tip position is controlled

DOI: 10.1021/acsami.9b04250
ACS Appl. Mater. Interfaces 2019, 11, 19286−19293

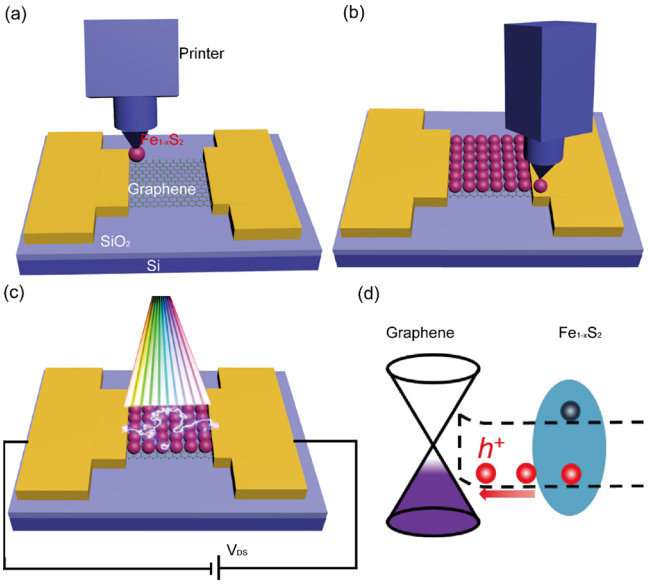

Figure 3. Schematic images of the printing process: (a) before and (b) after $Fe_{1-x}S_2$ NCs are printed on the GFET channel using an inkjet printer; (c) three-dimensional view of the printed LSPR $Fe_{1-x}S_2$ NCs/GFET broadband photodetector. (d) Energy level diagram of $Fe_{1-x}S_2$ NCs/GFET van der Waals heterojunction and charge transfer process under illumination.

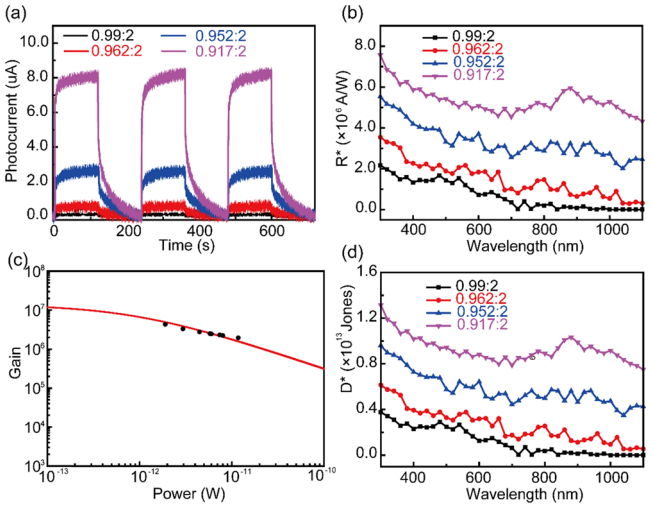

Figure 4. (a) Dynamic photoresponse I_D curves of the LSPR $Fe_{1-x}S_2$ NCs/GFET heterojunction photodetectors upon SWIR illumination (1100 nm) on and off. The light power density was 3.89 μW/cm^2. The GFET channel length and width are 4.3 and 11.4 μm, respectively. (b) Spectral photoresponsivity of the $Fe_{1-x}S_2$ NCs/GFET photodetectors. (c) Experimentally measured gain (black dots) versus theoretical fitting (red curve) as a function of the incident light power. (d) Wavelength-dependent broadband photodetectivity D^*.

by a computer (Figure 3b). Figure 3c illustrates a schematic image of a $Fe_{1-x}S_2$ NCs/GFET photodetector, in which the top two Au electrodes served as the source and drain. Charge transfer is a critical step affecting the optoelectronic properties of the $Fe_{1-x}S_2$ NCs/GFET UV−Vis−NIR broadband photodetectors. The vdW interface provides a high-efficiency charge transfer path across the interface as we reported in the ZnO QD/GFET heterojunction UV photodetector.[37] The charge transfer mechanism of the $Fe_{1-x}S_2$ NCs/GFET photodetector under illumination is shown in Figure 3d. Upon the absorption of light by the $Fe_{1-x}S_2$ NCs, excitons are generated and dissociated to free electrons and holes at the $Fe_{1-x}S_2$ NCs/GFET interface by the built-in field. Based on the band edge alignment across the $Fe_{1-x}S_2$ NCs/GFET interface shown in Figure 3d, the photoexcited charges (holes) in the valence band of $Fe_{1-x}S_2$ NCs are expected to transfer to graphene, leading to a photogating effect on the GFET channel conductance as the photoresponse.[37]

The $Fe_{1-x}S_2$ NCs/GFET vdW heterojunction photodetector exhibits excellent photoresponse reversibility. Figure 4a shows the on/off current density plots of the doped $Fe_{1-x}S_2$ NCs/GFET photodetectors (colored) under illumination of SWIR light of 1100 nm with a light power density of 3.89 μW/cm^2. For a comparison, the FeS_2 NCs/GFET photodetector with stoichiometric FeS_2 NCs (black) is also included in Figure 4a. For all devices, the source−drain bias voltage (V_{DS}) was maintained at 0.1 V. Remarkably, the devices with doped $Fe_{1-x}S_2$ NCs have significantly higher photoresponse than their counterpart with stoichiometric FeS_2 NCs. This is not surprising since SWIR photoresponse is forbidden, considering the bandgap of 1.58 eV for the stoichiometric FeS_2 NCs. This means that the observed SWIR photoresponse in doped $Fe_{1-x}S_2$ NCs/GFET photodetectors is primarily attributed to the LSPR effect through expansion of the absorption spectrum from visible toward longer wavelengths into SWIR, enabling broadband photodetection in the UV−Vis−SWIR spectrum.

The responsivity R^* is defined as the ratio of photocurrent (I_{ph}) to incident optical power (P_{in}) absorbed in the $Fe_{1-x}S_2$ NCs/GFET photodetector: $R^* = I_{ph}/P_{in}$. I_{ph} is defined as the difference between current under illumination and in the dark. Figure 4b compares the R^* versus wavelength curves on the four samples shown in Figure 4a. The R^* values of the doped $Fe_{1-x}S_2$ NCs/GFET photodetectors (colored) are considerably higher than those of their counterpart with stoichiometric FeS_2 NCs (black). The most significant R^* enhancement occurs in the NIR−SWIR spectrum. At an SWIR wavelength of 1100 nm, the enhancement is almost three orders of magnitude from 6.49×10^3 A/W at the Fe/S elemental ratio of 0.99:2 to 4.32×10^6 A/W at Fe/S = 0.917:2. Even at the UV wavelength of 300 nm, an almost 4-fold enhancement of the R^* can be seen in Figure 4b. It should be pointed out that the spectral responsivity in Figure 4b agrees well qualitatively with the UV−Vis−IR absorption spectra in Figure 2c, illustrating that the broadband enhancement of the photoresponse in the $Fe_{1-x}S_2$ NCs/GFET photodetectors is primarily ascribed to the LSPR effect on the doped $Fe_{1-x}S_2$ NCs photosensitizers. This result demonstrates the benefit of the enhanced LSPR absorption by doped $Fe_{1-x}S_2$ NCs in the $Fe_{1-x}S_2$ NCs/GFET vdW heterojunction photodetectors for broadband photodetection. At the optimal doping at $x = 0.083$, the $Fe_{0.917}S_2$ NCs exhibit the strongest LSPR effect (purple in Figure 2c), leading to the highest R^* values exceeding 4.0×10^6 A/W in UV−Vis−SWIR on the $Fe_{0.917}S_2$ NCs/GFET devices (purple curve in Figure 4b). This is in contrast to the much lower R^* of ~10^6 A/W for the stoichiometric $Fe_{0.99}S_2$ NCs/GFET device (black in Figure 4b) only from ultraviolet (300 nm) to visible (560 nm). However, the responsivity decreases monotonically with increasing wavelengths near or beyond the cutoff (785 nm) of the stoichiometric $Fe_{0.99}S_2$ NCs. The fact that R^* decreases by almost three orders of magnitude from 560 nm (below the cutoff) to 1100 nm beyond the cutoff, which is anticipated for traditional semiconductors such as the stoichiometric $Fe_{0.99}S_2$ NCs. Therefore, the enhanced broad-

DOI: 10.1021/acsami.9b04250
ACS Appl. Mater. Interfaces 2019, 11, 19286−19293

band responsivity on the $Fe_{1-x}S_2$ NCs/GFET photodetectors illustrates the unique advantage of the LSPR effect in the doped $Fe_{1-x}S_2$ NCs. Figure S4 shows the photoresponsivity of the $Fe_{1-x}S_2$ NCs/GFET photodetector as a function of the bias voltage V_{sd}. The linear increase of the responsivity with V_{sd} is anticipated since the carrier drift velocity between the source and drain electrodes increases linearly with V_{sd}.

It should be pointed out that the $Fe_{1-x}S_2$ NCs/GFET photodetectors take advantages of the improved LSPR absorption of doped $Fe_{1-x}S_2$ NCs, in combination with the strong quantum confinement in the highly crystalline $Fe_{1-x}S_2$ NCs for prolonged carrier lifetime (T_{life}) and the high charge mobility of graphene for a short source−drain charge transit time ($T_{transit}$). Therefore, high and broadband photoconductive gain (G) proportional to $T_{life}/T_{transit}$ is anticipated for $Fe_{1-x}S_2$ NCs/GFET phototransistors. To quantify this, the photoconductive gain in these $Fe_{1-x}S_2$ NCs/GFET vdW heterojunction photodetectors can be estimated from the following equation[37]

$$G = \frac{I_{ph}h\nu}{qiWL} = (a_0 qNVW)\frac{h\nu}{qiWL} = a_0 \emptyset \frac{T_{life}}{T_{transit}} \frac{1}{1+\left(\frac{i}{i_0}\right)^n} \quad (1)$$

Here, q is the elementary charge, i is the light power absorbed by $Fe_{1-x}S_2$ on the GFET channel, W and L are respectively the GFET channel width and length, a_0 is the photogenerated carrier transfer efficiency from the $Fe_{1-x}S_2$ NCs to graphene, and N is the Avogadro constant. The carrier drift velocity $V = \mu V_{DS}/L$ is proportional to the carrier mobility μ in graphene. In addition, $h\nu$ is the elemental photo energy, Ø is the quantum efficiency of $Fe_{1-x}S_2$ NCs, i_0 is the saturation light power on the NCs when all of the surface states are filled, and n is a phenomenological fitting parameter. Figure 4c plots the G versus i curve measured on the $Fe_{0.917}S_2$ NCs/GFET photodetector (black dots) and the theoretical fitting (red curve).[38] A maximum gain of 4.3×10^6 under an illumination power of 1.91 pW can be observed. With increasing incident light power beyond 1.91 pW, the gain decrease monotonically due to the reduced average lifetime of holes and saturation of the surface states. For the theoretical fitting curve shown in Figure 4b, the fitting parameters are $a_0\emptyset = 0.21$, $i_0 = 0.90$ pW, and $n = 0.80$. A further enhanced gain predicted from the theoretical calculation is as high as $\sim 1.19 \times 10^7$ under a low incident light power of <0.1 pW.

The detectivity (D^*) is a key figure of merit for a photodetector and can be calculated from the following equation[38]

$$D^* = \frac{\sqrt{A \times \Delta f}}{\mathrm{NEP}} \text{ (Jones)} \quad (2)$$

where A is the active layer of the $Fe_{1-x}S_2$ heterojunction photodetector in cm^2, Δf is the bandwidth in hertz, and NEP is the noise equivalent power in the unit of $A/Hz^{1/2}$, which indicates the incident light power required for the device output signal to be equal to the noise current. The NEP can be calculated using the formula $\mathrm{NEP} = \overline{A_n^2}^{1/2}/R^*$, where $\overline{A_n^2}$ is the mean square noise current and can be obtained from the spectra density of the noise power. The $\overline{A_n^2}$ of the $Fe_{1-x}S_2$ NCs/GFET device monotonically decreases with increasing frequency, which can be fitted by $\overline{A_n^2} \propto 1/f$ in the low frequency range up to hundreds of hertz, demonstrating that the $1/f$ noise dominates the current noise behavior at low frequencies (Figure S5). The wavelength-dependent D^* of the $Fe_{1-x}S_2$ NCs/GFET photodetectors is shown in Figure 4d. Among the four $Fe_{1-x}S_2$ NCs/GFET devices shown in Figure 4d (the same four devices as in Figure 4a,b), the three based on the doped $Fe_{1-x}S_2$ NCs (colored) have higher D^* values than those based on the stoichiometric $Fe_{0.99}S_2$ NCs (black) in the entire UV−Vis−NIR−SWIR spectra. The one with the Fe-to-S ratio of 0.917:2 (purple) has the overall highest D^* values in the entire UV−Vis−NIR−SWIR spectra. At short wavelengths below 340 nm, the D^* for the $Fe_{0.917}S_2$ NCs/GFET photodetector (purple) reaches up to 1.15×10^{13} Jones, which is significantly higher than the $D^* \approx 3.1 \times 10^{12}$ Jones of its counterpart based on the stoichiometric $Fe_{0.99}S_2$ NCs (black). While it decreases with increasing wavelengths for all four samples, the D^* value of 7.50×10^{12} Jones of the $Fe_{0.917}S_2$ NCs/GFET photodetector is more than two orders of magnitude higher than the 1.1×10^{10} Jones of the $Fe_{0.99}S_2$ NCs/GFET counterpart.

It should be pointed out that the LSPR-enhanced light absorption in doped $Fe_{1-x}S_2$ NCs addresses a fundamental issue in photodetectors based on semiconductor NCs due to the limited absorption in a thin layer of the stoichiometric semiconductor NCs. A naive resolution is to stack NCs to multilayers for enhanced light absorption, as shown in Figure 5a. Unfortunately, charge transfer across the stacked semiconductor NC layers is seriously hindered by the poorly defined NC−NC interfaces, and the difference in the charge transfer routes in the multilayered NCs/graphene and single-layered NCs/graphene heterostructures is illustrated in Figure 5a,b. Basically, The photogenerated holes on the top NC layers in the multilayered NCs (Figure 5a) must go through multiple

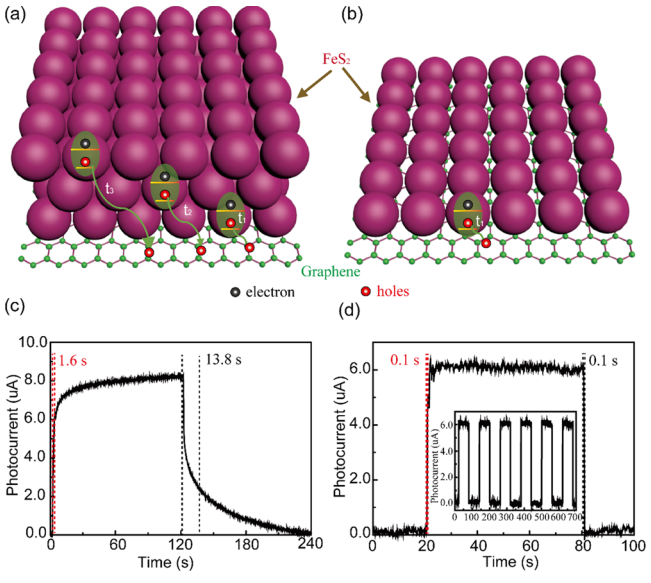

Figure 5. Schematic diagrams of photo-induced charge carrier transport paths in (a) multilayer and (b) single layer (or thinner layer) of $Fe_{1-x}S_2$ NCs/GFET photodetectors. The corresponding dynamic photoresponse in the devices with (c) a multilayer and (d) single-layer (d) $Fe_{1-x}S_2$ NCs sensitizer. The rising (falling) time is estimated from the time required for the photocurrent to increase to (decrease to) 70% of the maximum value of the photocurrent. The inset in (d) shows the time-dependent on/off current density of the single-layer $Fe_{1-x}S_2$ NCs photodetector.

DOI: 10.1021/acsami.9b04250
ACS Appl. Mater. Interfaces 2019, 11, 19286−19293

NC−NC interface junctions before reaching to graphene. In contrast, a direct charge transfer from NC to graphene can be achieved in the single-layered NC case (Figure 5b). This difference in the charge transfer route results in a direct consequence of slower photoresponse due to charge traps at the NC−NC interface junctions in the $Fe_{1-x}S_2$ NCs/GFET devices with a multilayered $Fe_{1-x}S_2$ NC sensitizer. This argument is indeed supported by the dramatically slower and smaller dynamic photoresponse of the $Fe_{1-x}S_2$ NCs/GFET photodetectors with multilayers of the $Fe_{1-x}S_2$ NCs (Figure 5c) as compared to its single-layer counterpart (Figure 5d). The thicknesses of the multilayer and single-layer NC samples used in Figure 5c,d are ∼540 and 60 nm, respectively (Figure S6). While the photocurrent of 8.24 μA in the former is about 1.3 times of the 6.16 μA in the latter, the photoresponse is significantly slower in the former. To quantify this, the rising (falling) time is estimated from the time required for the photocurrent to increase to (decrease to) 70% of the light on-state current. In fact, an asymmetric rise/fall pattern can be observed in the $Fe_{1-x}S_2$ NCs/GFET devices with a multilayered $Fe_{1-x}S_2$ NCs sensitizer. As illustrated in Figure 5c, the rising time of ∼1.6 s in response to the illumination of the SWIR (1100 nm) "light on" is almost an order of magnitude shorter than the falling time of ∼13.8 s in response to the "light off". In contrast, the rising and falling times are both ∼0.1 s in the $Fe_{1-x}S_2$ NCs/GFET devices with single-layered $Fe_{1-x}S_2$ NCs. Therefore, the slower and asymmetric photoresponse in the $Fe_{1-x}S_2$ NCs/GFET photodetectors with a multilayered $Fe_{1-x}S_2$ NCs sensitizer indicates the presence of charge traps most probably at the NC−NC interface junctions.[37] Besides the detrimental effect on the response times, these charge traps also promote charge recombination and reduce the photoresponse. This argument is consistent with only 30% higher photocurrent in the multilayered $Fe_{1-x}S_2$ NCs of thickness (540 nm) nine times of that on the single-layered NC sample. Therefore, the significantly faster and symmetric photoresponse and the specific response (per NC thickness) in the single-layer $Fe_{1-x}S_2$ NCs/graphene illustrate the importance of the LSPR effect in doped $Fe_{1-x}S_2$ NCs/GFET for high-performance optoelectronic devices. The inset in Figure 5d demonstrates the on/off current density of the single-layer $Fe_{1-x}S_2$ NCs/GFET photodetector in response to six cycles of the light on and light off. A stable photocurrent can be retained during the process, demonstrating the stability of the photodetector.

4. CONCLUSIONS

In summary, a colloidal process was developed for synthesis of highly crystalline nonstoichiometric $Fe_{1-x}S_2$ NCs with a systematically controlled hole doping for the LSPR effect by introduction of Fe deficiencies in the range of $x = 0.01-0.107$. By increasing doping x up to 0.083, a systematic increase in the absorption intensity and spectral range of UV−Vis−SWIR, which is much beyond the visible cutoff of ∼785 nm of the stoichiometric FeS_2 NCs, has been obtained. At the optimal doping of $x = 0.083$, the free carrier density is estimated to be 1.91×10^{22} cm^{-3}. A further increase in the doping leads to reduced absorption intensity, which may be attributed to the enhanced light reflection in more metallic $Fe_{1-x}S_2$ NCs. The LSPR effect in the doped $Fe_{1-x}S_2$ NCs provides a unique resolution to the critical issue of inadequate light absorption in the optoelectronic devices with a thin layer of semiconductor NCs. This advantage is demonstrated in a comparative study of the $Fe_{1-x}S_2$ NCs/GFET photodetectors with stoichiometric ($x = 0.01$) and doped (x is up to 0.083) $Fe_{1-x}S_2$ NCs. In contrast to the much lower $R^* \approx 10^6$ A/W for the stoichiometric $Fe_{0.99}S_2$ NCs/GFET device below the cutoff of 785 nm, a remarkable broadband R^* exceeding 4.32×10^6 A/W and detectivity D^* of $>7.50 \times 10^{12}$ Jones are observed in nonstoichiometric $Fe_{1-x}S_2$ NCs/GFET (optimal $x = 0.083$). The enhanced R^*, especially that at NIR to SWIR wavelengths beyond the cutoff, should be attributed to the synergistic combination of the enhanced LSPR light absorption, strong quantum confinement of the $Fe_{1-x}S_2$ NC sensitizer, and high carrier mobility of the graphene for high-performance optoelectronics. This result is important as demonstrated in a further comparative study of $Fe_{1-x}S_2$ NCs/GFET devices with 60 nm-thick (single-layer) and 540 nm-thick (multilayer) $Fe_{1-x}S_2$ NCs as photosensitizers. While the latter has 30% higher R^* than in the former, its response times increase by more than an order of magnitude due to the charge trapping effect at the NC−NC junctions through multiple layers of $Fe_{1-x}S_2$ NCs. Therefore, this result demonstrates a pathway toward printable and flexible high-performance optoelectronics.

■ ASSOCIATED CONTENT

Supporting Information

The Supporting Information is available free of charge on the ACS Publications website at DOI: 10.1021/acsami.9b04250.

TEM images of $Fe_{1-x}S_2$ NCs with different chemical compositions, optical and microscope optical images of a patterned GFET chip, Raman spectrum of graphene and $Fe_{1-x}S_2$ NCs/graphene, photoresponsivity as a function of the bias voltage, spectra of current noise density of GFET and $Fe_{1-x}S_2$ NCs/GFET devices, thickness of multilayer and single-layer $Fe_{1-x}S_2$ NCs films, elemental ratios of Fe to S, and comparison of the performance of broadband photodetectors (PDF)

■ AUTHOR INFORMATION

Corresponding Authors

*E-mail: gmg@ku.edu (M.G.).
*E-mail: jwu@ku.edu (J.Z.W.).

ORCID

Maogang Gong: 0000-0002-2031-781X

Notes

The authors declare no competing financial interest.

■ ACKNOWLEDGMENTS

We thank the support by Plant Directed Research and Development funds from the Department of Energy's National Security Campus, operated and managed by Honeywell Federal Manufacturing and Technologies, LLC, under contract no. DE-NA0002839. This research was also supported, in part, by ARO contract no. W911NF-16-1-0029 and NSF contract nos. NSF-ECCS-1809284/1809293 and NSF-DMR-1508494.

■ REFERENCES

(1) Hu, K.; Chen, H.; Jiang, M.; Teng, F.; Zheng, L.; Fang, X. Broadband Photoresponse Enhancement of a High-Performancet-Se Microtube Photodetector by Plasmonic Metallic Nanoparticles. *Adv. Funct. Mater.* **2016**, *26*, 6641−6648.

DOI: 10.1021/acsami.9b04250
ACS Appl. Mater. Interfaces 2019, 11, 19286−19293

(2) Chen, H.; Su, L.; Jiang, M.; Fang, X. Highly Desirable Photodetectors Derived from Versatile Plasmonic Nanostructures. *Adv. Funct. Mater.* **2017**, *27*, 1704181.
(3) Mei, C.; Liu, S.; Huang, X.; Gan, Z.; Zhou, P.; Wang, H. Localized Surface Plasmon Induced Position-Sensitive Photodetection in Silicon-Nanowire-Modified Ag/Si. *Small* **2017**, *13*, 1701726.
(4) Sun, T.; Wang, Y.; Yu, W.; Wang, Y.; Dai, Z.; Liu, Z.; Shivananju, B. N.; Zhang, Y.; Fu, K.; Shabbir, B.; Ma, W.; Li, S.; Bao, Q. Flexible Broadband Graphene Photodetectors Enhanced by Plasmonic Cu_{3-x} P Colloidal Nanocrystals. *Small* **2017**, *13*, 1701881.
(5) Xu, G.; Lu, R.; Liu, J.; Chiu, H.-Y.; Hui, R.; Wu, J. Z. Photodetection based on Ionic Liquid Gated Plasmonic Ag Nanoparticle/ Graphene Nanohybrid Field Effect Transistors. *Adv. Opt. Mater.* **2014**, *2*, 729−736.
(6) Lu, R.; Konzelmann, A.; Xu, F.; Gong, Y.; Liu, J.; Liu, Q.; Xin, M.; Hui, R.; Wu, J. Z. High Sensitivity Surface Enhanced Raman Spectroscopy of R6G on in situ Fabricated Au Nanoparticle/ Graphene Plasmonic Substrates. *Carbon* **2015**, *86*, 78−85.
(7) Pillai, S.; Catchpole, K. R.; Trupke, T.; Green, M. A. Surface Plasmon Enhanced Silicon Solar Cells. *J. Appl. Phys.* **2007**, *101*, No. 093105.
(8) Cui, J.; Chen, C.; Han, J.; Cao, K.; Zhang, W.; Shen, Y.; Wang, M. Surface Plasmon Resonance Effect in Inverted Perovskite Solar Cells. *Adv. Sci.* **2016**, *3*, 1500312.
(9) Atwater, H. A.; Polman, A. Plasmonics for Improved Photovoltaic Devices. *Nat. Mater.* **2010**, *9*, 205−213.
(10) Hou, W.; Cronin, S. B. A Review of Surface Plasmon Resonance-Enhanced Photocatalysis. *Adv. Funct. Mater.* **2013**, *23*, 1612−1619.
(11) Zhou, H.; Liu, J.; Xu, J.-J.; Zhang, S.-S.; Chen, H.-Y. Optical Nano-Biosensing Interface via Nucleic Acid Amplification Strategy: Construction and Application. *Chem. Soc. Rev.* **2018**, *47*, 1996−2019.
(12) Miao, J.; Hu, W.; Jing, Y.; Luo, W.; Liao, L.; Pan, A.; Wu, S.; Cheng, J.; Chen, X.; Lu, W. Surface Plasmon-Enhanced Photodetection in Few Layer MoS_2 Phototransistors with Au Nanostructure Arrays. *Small* **2015**, *11*, 2392−2398.
(13) Liu, Y.; Cheng, R.; Liao, L.; Zhou, H.; Bai, J.; Liu, G.; Liu, L.; Huang, Y.; Duan, X. Plasmon Resonance Enhanced Multicolour Photodetection by Graphene. *Nat. Commun.* **2011**, *2*, 579.
(14) Luther, J. M.; Jain, P. K.; Ewers, T.; Alivisatos, A. P. Localized Surface Plasmon Resonances Arising from Free Carriers in Doped Quantum Dots. *Nat. Mater.* **2011**, *10*, 361−366.
(15) Kirkeminde, A.; Scott, R.; Ren, S. All Inorganic Iron Pyrite Nano-Heterojunction Solar Cells. *Nanoscale* **2012**, *4*, 7649−7654.
(16) Wang, J.-J.; Xue, D.-J.; Guo, Y.-G.; Hu, J.-S.; Wan, L.-J. Bandgap Engineering of Monodispersed $Cu_{2-x}S_ySe_{1-y}$ Nanocrystals through Chalcogen Ratio and Crystal Structure. *J. Am. Chem. Soc.* **2011**, *133*, 18558−18561.
(17) Erwin, S. C.; Zu, L.; Haftel, M. I.; Efros, A. L.; Kennedy, T. A.; Norris, D. J. Doping Semiconductor Nanocrystals. *Nature* **2005**, *436*, 91−94.
(18) Lo, S. S.; Mirkovic, T.; Chuang, C.-H.; Burda, C.; Scholes, G. D. Emergent Properties Resulting from Type-II Band Alignment in Semiconductor Nanoheterostructures. *Adv. Mater.* **2011**, *23*, 180−197.
(19) Dorfs, D.; Härtling, T.; Miszta, K.; Bigall, N. C.; Kim, M. R.; Genovese, A.; Falqui, A.; Povia, M.; Manna, L. Reversible Tunability of the Near-Infrared Valence Band Plasmon Resonance in $Cu_{2-x}Se$ Nanocrystals. *J. Am. Chem. Soc.* **2011**, *133*, 11175−11180.
(20) Kriegel, I.; Jiang, C.; Rodríguez-Fernández, J.; Schaller, R. D.; Talapin, D. V.; da Como, E.; Feldmann, J. Tuning the Excitonic and Plasmonic Properties of Copper Chalcogenide Nanocrystals. *J. Am. Chem. Soc.* **2012**, *134*, 1583−1590.
(21) Gong, M.; Adhikari, P.; Gong, Y.; Wang, T.; Liu, Q.; Kattel, B.; Ching, W.-Y.; Chan, W.-L.; Wu, J. Z. Polarity-Controlled Attachment of Cytochrome C for High-Performance Cytochrome C/Graphene van der Waals Heterojunction Photodetectors. *Adv. Funct. Mater.* **2018**, *28*, 1704797.
(22) Agrawal, A.; Cho, S. H.; Zandi, O.; Ghosh, S.; Johns, R. W.; Milliron, D. J. Localized Surface Plasmon Resonance in Semiconductor Nanocrystals. *Chem. Rev.* **2018**, *118*, 3121−3207.
(23) Wang, F.; Li, Q.; Lin, L.; Peng, H.; Liu, Z.; Xu, D. Monodisperse Copper Chalcogenide Nanocrystals: Controllable Synthesis and the Pinning of Plasmonic Resonance Absorption. *J. Am. Chem. Soc.* **2015**, *137*, 12006−12012.
(24) Han, W.; Yi, L.; Zhao, N.; Tang, A.; Gao, M.; Tang, Z. Synthesis and Shape-Tailoring of Copper Sulfide-Indium Sulfide-Based Nanocrystals. *J. Am. Chem. Soc.* **2008**, *130*, 13152−13161.
(25) Zhuang, Z.; Peng, Q.; Zhang, B.; Li, Y. Controllable Synthesis of Cu_2S Nanocrystals and Their Assembly into a Superlattice. *J. Am. Chem. Soc.* **2008**, *130*, 10482−10483.
(26) Sigman, M. B.; Ghezelbash, A.; Hanrath, T.; Saunders, A. E.; Lee, F.; Korgel, B. A. Solventless Synthesis of Monodisperse Cu_2S Nanorods, Nanodisks, and Nanoplatelets. *J. Am. Chem. Soc.* **2003**, *125*, 16050−16057.
(27) Riha, S. C.; Johnson, D. C.; Prieto, A. L. Cu_2Se Nanoparticles with Tunable Electronic Properties due to a Controlled Solid-State Phase Transition Driven by Copper Oxidation and Cationic Conduction. *J. Am. Chem. Soc.* **2011**, *133*, 1383−1390.
(28) Macpherson, H. A.; Stoldt, C. R. Iron Pyrite Nanocubes Size and Shape Considerations for Photovoltaic Application. *ACS Nano* **2012**, *6*, 8940−8949.
(29) Bi, Y.; Yuan, Y.; Exstrom, C. L.; Darveau, S. A.; Huang, J. Air Stable, Photosensitive, Phase Pure Iron Pyrite Nanocrystal Thin Films for Photovoltaic Application. *Nano Lett.* **2011**, *11*, 4953−4957.
(30) Shukla, S.; Xing, G.; Ge, H.; Prabhakar, R. R.; Mathew, S.; Su, Z.; Nalla, V.; Venkatesan, T.; Mathews, N.; Sritharan, T.; Sum, T. C.; Xiong, Q. Origin of Photocarrier Losses in Iron Pyrite (FeS_2) Nanocubes. *ACS Nano* **2016**, *10*, 4431−4440.
(31) Wu, L.; Dzade, N. Y.; Gao, L.; Scanlon, D. O.; Öztürk, Z.; Hollingsworth, N.; Weckhuysen, B. M.; Hensen, E. J. M.; de Leeuw, N. H.; Hofmann, J. P. Enhanced Photoresponse of FeS_2 Films: The Role of Marcasite-Pyrite Phase Junctions. *Adv. Mater.* **2016**, *28*, 9602−9607.
(32) Gong, M.; Kirkeminde, A.; Xie, Y.; Lu, R.; Liu, J.; Wu, J. Z.; Ren, S. Iron Pyrite (FeS_2) Broad Spectral and Magnetically Responsive Photodetectors. *Adv. Opt. Mater.* **2013**, *1*, 78−83.
(33) Wang, D.-Y.; Jiang, Y.-T.; Lin, C.-C.; Li, S.-S.; Wang, Y.-T.; Chen, C.-C.; Chen, C.-W. Solution-Processable Pyrite FeS_2 Nanocrystals for the Fabrication of Heterojunction Photodiodes with Visible to NIR Photodetection. *Adv. Mater.* **2012**, *24*, 3415−3420.
(34) Gong, M.; Kirkeminde, A.; Ren, S. Symmetry-Defying Iron Pyrite (FeS_2) Nanocrystals through Oriented Attachment. *Sci. Rep.* **2013**, *3*, 2092.
(35) Zhang, X.; Xu, Y.; Guo, G.; Ji, C.; Tao, H.; Shen, L.; Bao, N. Tuning Localized Surface Plasmon Resonances of FeS_2 Nanocrystals via Shape and Surface Functional Groups for Enhanced Photoconductivity. *J. Mater. Sci.: Mater. Electron.* **2017**, *28*, 12717−12725.
(36) Gong, M.; Sakidja, R.; Liu, Q.; Goul, R.; Ewing, D.; Casper, M.; Stramel, A.; Elliot, A.; Wu, J. Z. Broadband Photodetectors Enabled by Localized Surface Plasmonic Resonance in Doped Iron Pyrite Nanocrystals. *Adv. Opt. Mater.* **2018**, *6*, 1701241.
(37) Gong, M.; Liu, Q.; Cook, B.; Kattel, B.; Wang, T.; Chan, W.-L.; Ewing, D.; Casper, M.; Stramel, A.; Wu, J. Z. All-Printable ZnO Quantum Dots/Graphene van der Waals Heterostructures for Ultrasensitive Detection of Ultraviolet Light. *ACS Nano* **2017**, *11*, 4114−4123.
(38) Gong, M.; Sakidja, R.; Goul, R.; Ewing, D.; Casper, M.; Stramel, A.; Elliot, A.; Wu, J. Z. High-Performance All-Inorganic $CsPbCl_3$ Perovskite Nanocrystal Photodetectors with Superior Stability. *ACS Nano* **2019**, *13*, 1772−1783.
(39) Gong, M.; Liu, Q.; Goul, R.; Ewing, D.; Casper, M.; Stramel, A.; Elliot, A.; Wu, J. Z. Printable Nanocomposite FeS_2-PbS Nanocrystals/Graphene Heterojunction Photodetectors for Broadband Photodetection. *ACS Appl. Mater. Interfaces* **2017**, *9*, 27801−27808.

DOI: 10.1021/acsami.9b04250
ACS Appl. Mater. Interfaces 2019, 11, 19286−19293

(40) Tauc, J. Optical Properties and Electronic Structure of Amorphous Ge and Si. *Mater. Res. Bull.* **1968**, *3*, 37−46.
(41) Manthiram, K.; Alivisatos, A. P. Tunable Localized Surface Plasmon Resonances in Tungsten Oxide Nanocrystals. *J. Am. Chem. Soc.* **2012**, *134*, 3995−3998.

DOI: 10.1021/acsami.9b04250
ACS Appl. Mater. Interfaces 2019, 11, 19286−19293